Appl. Phys. B 86, 249–258 (2007)
DOI: 10.1007/s00340-006-2441-5

**Applied Physics B**
**Lasers and Optics**

D.E. ROSKEY[1,✉]
M. KOLESIK[1,2]
J.V. MOLONEY[1,2]
E.M. WRIGHT[1,2]

# The role of linear power partitioning in beam filamentation

[1] College of Optical Science, University of Arizona, Tucson, AZ 85721, USA
[2] Arizona Center for Mathematical Sciences, University of Arizona, Tucson, AZ 85721, USA

**Received: 17 May 2006/Revised version: 29 July 2006**
**Published online: 9 September 2006 • © Springer-Verlag 2006**

**ABSTRACT** We demonstrate through computer simulation that power partitioning due to linear diffraction can play a crucial role in the break up of high intensity apertured beams propagating in air. By investigating the way linear diffraction partitions power in these beams, we are able to predict the positions and relative powers of supercritical hot spots.

**PACS** 42.65.k; 42.65.Jx

## 1 Introduction

Nonlinear beam filamentation and self-guiding are areas of increasingly vigorous research, the behavior of collimated initial beams with Gaussian profiles having been studied extensively. It is well known that these beams undergo collapse at and above a certain critical power $P_{cr}$ [1], and for pulsed beams this collapse is regularized by a combination of diffraction, plasma induced defocusing and group velocity dispersion (GVD) [2–4]. For propagation in air, pulses with peak powers a few times the critical power can form spatially confined light filaments whose fluence profiles remain almost constant over long distances [7]. Several models were proposed to explain this long distance propagation including the moving focus model by Brodeur et al. [8], the self-waveguiding model by Lange et al. [9] and dynamic spatial replenishment by Mlejnek et al. [10, 11].

At peak pulse powers many times the critical power, it has been demonstrated that multiple filaments are formed [7, 12, 14]. Much work has gone into understanding the nature of filamentation and the processes leading to beam break up into multiple filaments. For beams of a few critical powers, global approaches such as the virial theorem applied to the beam Hamiltonian have proven useful in describing the global dynamics of filamentation [1, 5, 6]. For beams that are many times the critical power, multiple filamentation has been studied in terms of modulation instability (MI) and in terms of filament nucleation around stochastic and deterministic perturbations in the initial beam [13–15]. However, as we will discuss shortly, the virial theorem cannot address hot spot formation in the absence of whole beam collapse and MI analysis is frequently insufficient to describe filamentation in supercritical beams [16, 17]. Additionally, several groups have done work recently that show that filamentation can be controlled to a degree using apodization [18–20], linear aberrations [21] and optical squeezing with a telescope [22].

In this paper, we build upon an idea first recognized by Campillo et al.[23] and later utilized by Kandidov et al. in their work to control multiple filamentation using a metallic mesh [19]. Specifically, we investigate the idea that linear diffraction can exert a dominant influence on initial partitioning of power in nonlinear beams thereby deterministically arranging multiple filaments in supercritical beams. This effect is especially apparent in beams that are highly aberrated or that have profiles with hard edges. Such beams strongly deviate from collimated beams with single bell-shaped maxima and are highly multi-moded and hence not amenable to the standard MI analysis of filamentation. Though MI analysis may be applicable in principle to these cases, linear diffraction alters the beam profile faster than does nonlinear unstable mode growth making it impractical. Eventually, enough power is partitioned into one or more hot spots, and the nonlinear processes become dominant in the critical and supercritical spots. Subsequently, the evolution of each hot spot is similar to that of an isolated, single filament. We contend that simple linear analysis yields accurate results and is more transparent conceptually than MI analysis for these cases.

In this paper our goal is to present examples elucidating the role of linear power partitioning in beam filamentation in air for the case of apertured, or apodized, input beams. However, the approach that is proposed is applicable to beams with strong phase aberrations as well. We outline the basic theory we shall refer to for continuous wave (cw) beams in Sect. 2, and then turn to cw simulations in Sect. 3 to illustrate the role of linear partitioning in high power beams. Section 4 is devoted to pulsed simulations in order to demonstrate that our physical picture of linear partitioning has relevance to short pulse propagation in air. Finally, our summary and conclusions are given in Sect. 5.

## 2 Basic theory

Our starting point is the nonlinear Schrödinger equation (NLS) for the scalar electric field envelope $E(\boldsymbol{r})$ of a cw field of frequency $\omega$ propagating dominantly along the

✉ Fax: +1-520 621 1510, E-mail: droskey@optics.arizona.edu

$z$-axis [10]

$$\frac{\partial E}{\partial z} = \frac{\mathrm{i}}{2k}\nabla_t^2 E + \mathrm{i}k_0 n_2 |E|^2 E\,, \tag{1}$$

where $k = n_\mathrm{b}\omega/c = n_\mathrm{b}k_0$ is the magnitude of the wavevector, $n_\mathrm{b}$ being the background refractive index, $\nabla_t^2$ is the transverse Laplacian, $\boldsymbol{r} = (\boldsymbol{r}_t, z) = (x, y, z)$ and $n_2$ is the nonlinear Kerr coefficient in air. Here the field envelope is scaled so that $|E|^2$ is an intensity.

### 2.1 *Virial theorem*

The virial theorem is based on two integrals of motion of the NLS (1), namely the beam Hamiltonian [1, 5, 24]

$$H = \frac{1}{4k^2}\int \mathrm{d}^2\boldsymbol{r}_t \left\{|\nabla_t E|^2 - kk_0 n_2 |E|^4\right\}\,, \tag{2}$$

and the beam power

$$P = \int \mathrm{d}^2\boldsymbol{r}_t |E(\boldsymbol{r}_t, z)|^2\,. \tag{3}$$

Then, according to the virial theorem, the mean-square (MS) spot size of the beam, calculated as

$$\langle r^2(z)\rangle = \frac{1}{P}\int \mathrm{d}^2\boldsymbol{r}_t (x^2 + y^2)|E(\boldsymbol{r}_t, z)|^2\,, \tag{4}$$

evolves according to [5, 24]

$$\frac{\mathrm{d}^2\langle r^2\rangle}{\mathrm{d}z^2} = \frac{8H}{P}\,, \tag{5}$$

with solution

$$\langle r^2(z)\rangle = \langle r^2(0)\rangle + \frac{\mathrm{d}\langle r^2\rangle}{\mathrm{d}z}\,|_{z=0}\, z + \frac{4H}{P}z^2\,. \tag{6}$$

Then for the case $H < 0$, the mean-square beam size must eventually go towards zero giving rise to global or whole beam collapse. If $H > 0$, however, the outcome is not as clear as it is not possible to rule out collapse based on a positive Hamiltonian alone. Local hot spots with powers exceeding the critical value can still occur leading to localized collapse [1]. Thus, by itself the virial theorem cannot resolve whether local collapse can occur in the absence of whole beam collapse.

For more on the virial theorem and how it applies to blow-up of the nonlinear Schrödinger equation see Rasmussen et al. [5]. For more on how the virial theorem applies to collapse of space-time pulses see Bergé et al. [14].

### 2.2 *Nucleation of multiple filaments*

Multiple filaments can form in broad beams that contain many times the critical power. In some cases, the multiple filaments may be nucleated by stochastic perturbations imposed on the laser beam. These perturbations may come from shot-to-shot fluctuations in the laser system, turbulence or some other random non-uniformity in the nonlinear medium. Shot-to-shot variations are difficult to deal with from an a priori stand-point and must be handled with statistical methods [25]. However, it is frequently the case that filaments form fairly robust patterns that are repeatable from shot to shot [15] so that systematic but perhaps unintended aberrations within the laser system drive the beam filamentation instead of stochastic perturbations. Furthermore, even in the presence of stochastic perturbations, the noise and modulation instability still need not dominate the filamentation process [16, 17].

The significance of atmospheric turbulence for the simulations presented here can be estimated by following the method of Fried [26, 27]. For a propagation length $L$, Fried defines a coherence length for atmospheric turbulence given by

$$r_0 \approx \left(\frac{6.88}{\mathcal{A}}\right)^{3/5}\,, \tag{7}$$

with

$$\mathcal{A} = 2.91 k_0^2 C_N^2 L\,, \tag{8}$$

where $k_0$ is the vacuum wavenumber, $C_N$ is the atmospheric refractive-index structure constant and typically ranges between $10^{-13}$–$10^{-14}\,\mathrm{m}^{-2/3}$ near the surface of the earth [28]. As a concrete example we consider horizontal propagation at fixed altitude and set $C_N = 1\times 10^{-13}\,\mathrm{m}^{-2/3}$. Taking $\lambda =$ 789 nm, substituting (8) into (7) and solving for $L$ gives

$$L = \left(\frac{0.6}{r_0}\right)^{5/3}\,. \tag{9}$$

Thus, for an incident optical beam with a characteristic width $D$, we would expect turbulence to significantly affect its propagation over a length $L$ only when the turbulence coherence length is close to the beam diameter, $r_0 \approx D$. This occurs after the beam has propagated a distance given by $L = \left(\frac{0.6}{D}\right)^{5/3}$. For $D = 1$ cm this occurs at a propagation distance of about 1 km. The simulations in this paper deal with beams that are much less that 1 cm in diameter and exhibit linear diffractive effects that operate over distances of no more than a few meters. Thus, we can safely neglect turbulence effects here. Other inhomogeneities, such as water droplets, can affect the beam. We also neglect these effects here. Other groups have studied the impact of turbulence [29] and water droplets [30] on the filamentation process.

Bergé et al. have done extensive work exploring the impact of stochastic and non-stochastic perturbations on multiple filament patterns in supercritical beams [14]. Their work focused on circularly symmetric Gaussian and superGaussian beams with small initial perturbations. These perturbations seeded unstable modes which subsequently grew, leading to filamentation.

Here we consider the case of non-axisymmetric beams in which the filamentation is dominated by linear diffraction caused by the apodization of the incident field. Initial perturbations, stochastic and deterministic, are neglected in this study.

### 2.3 *Motivation for linear analysis*

The two overarching processes in multiple filamentation of beams are power partitioning followed by nonlinear

propagation. Diffraction often plays a pivotal role in partitioning the beam. In many cases, diffraction partitions beam power more quickly than do small perturbations and unstable mode growth. In this paper, we are concerned with beam power partitioning due primarily to diffraction. We have developed a procedure by which patterns of multiple hot spots in supercritical beams can be determined to a high degree of accuracy using a relatively small amount of computational resources. This procedure consists of first propagating the beam linearly, allowing diffraction to partition the beam. At various stages of propagation, the beam profile is examined for potential bell-shaped hot spots. The fraction of the total beam power partitioned in each hot spot by linear diffraction is computed. This information along with the total input peak power can be used to determine whether or not a given hot spot will become supercritical during propagation. Supercritical bell-shaped hot spots would lend themselves to self-similar collapse in the absence of a collapse-regularizing mechanism. Therefore, hot spots that become supercritical will likely persist as filaments whereas the subcritical spots will continue to diffract and spread.

Using this procedure we are able to show that linear diffraction plays a dominant role in deterministically arranging the filaments in a wide range of supercritical beams. We contend that these results are applicable to real, high power optical systems and experiments, and this assertion is born out by recent experiments [18, 19, 21].

## 3 Continuous wave simulations

We start by presenting two-dimensional (2D) cw nonlinear beam propagation simulations. Full space-time simulations were also performed and will be discussed later in this article.

In order to demonstrate the process of power partitioning, a number of 2D cw simulations were performed for a variety of initial beam profiles, and the resulting nonlinear beam profiles were studied at various steps in the propagation and compared with similar positions in the linear profiles. The initial beam profiles that were studied were a square eighth-order super-Gaussian beam and an irregularly shaped beam, both having an initial flat phase profile. (The eight-order super-Gaussian is intended to simulate a square aperture and was used in place of a hard aperture to allow analytic evaluation of the beam Hamiltonian for this example.) All the simulations were carried out using a split-step, pseudo-spectral algorithm [31] within the slowly varying amplitude approximation [32]. The simulations employed the parameters for air for a free-space wavelength of $\lambda = 789\,\text{nm}$, $n_\text{b} = 1$, and $n_2 = 5.57 \times 10^{-23}\,\text{m}^2\text{W}^{-1}$, which corresponds to a critical power ($P_\text{cr}$) of 1.8 GW where $P_\text{cr} = \frac{\lambda^2}{2\pi n_\text{b} n_2}$.

Because these were cw simulations, no temporal or dispersion effects such as plasma induced defocusing or GVD were included. For this reason, the simulations can be regarded as physically relevant for a given hot spot only up to the point of that spot's collapse. In the context of this study, collapse was assumed to occur when a given hot spot reached an intensity of $1 \times 10^{18}\,\text{Wm}^{-2}$. In some cases, it was desirable to continue the cw simulation past a particular spot's collapse in order to determine if other collapse events occurred. In these cases a Kerr saturation model was employed to artificially regulate collapse. Saturation was incorporated by replacing the Kerr term $n_2|E|^2$ in (1) with the Kerr saturation term $\frac{n_2|E|^2}{1+|E|^2/|E_\text{sat}|^2}$, where $|E_{sat}|^2 = 10^{18}\,\text{Wm}^{-2}$.

### 3.1 *Square beam profile*

Figure 1 shows the linear diffraction patterns of a $4 \times 4\,\text{mm}^2$ square aperture at propagation distances ranging from 0.3–6.0 m. The beam was modelled as an eighth-order super-Gaussian in the transverse coordinates

$$E(x, y, z = 0) = E_0 \exp\left[-\left(\frac{x}{d}\right)^{2m} - \left(\frac{y}{d}\right)^{2m}\right] \tag{10}$$

where $m = 8$ and $d = 2\,\text{mm}$. The first step in our procedure is to inspect the results of the linear propagation and locate potential bell-shaped hot spots. In Fig. 1d for $z = 2$ m approximately 12% of the beam power is concentrated in each of the four corner lobes, 9% in the centered side lobes and 7% in the central peak of the beam. In Fig. 1e for $z = 3$ m about 20% of the power is contained in each of the four lobes. Therefore, we expect that the corner spots in Fig. 1d would be candidates for filamentation if 12% of the total beam power was a supercritical power. For our simulations here, this required the beam to carry at least 15 GW. Likewise, the center side spots in Fig. 1d require a total beam power of at least 20 GW to be supercritical. However, the spots in Fig. 1e would be filament candidates for beams of only 9 GW or more. So, for this example, we would expect the beam to break up in a patter like that in Fig. 1e if the total beam power was between about 9 GW and 20 GW. For powers a little above 20 GW, we would expect to see a filamentation pattern like that in Fig. 1d. For powers significantly larger than 20 GW ($\approx 30$ GW), a more complex pattern with a greater number of filaments would result. For powers much below 9 GW, the result would be a single self-focusing hot spot or none at all.

Nonlinear cw simulations were performed with this square aperture for two different total beam powers of 9.2 GW and 25 GW. Using the information obtained from the linear propagation, it is possible to determine the relative distribution and strengths of self-focusing hot spots in each of these two cases. For a 9.2 GW beam we expect local collapse to start at around $z = 3$ m on the four corner lobes, corresponding to Fig. 1e (3.0 m). This is so since linear diffraction has partitioned the power so that about 20% is concentrated in each of the four lobes, which for a 9.2 GW input beam gives just over a critical power $P_\text{cr} = 1.8$ GW in each lobe. Prior to this distance, no bell-shaped hot spots were found with sufficient power to produce sustained local collapse. Therefore, before $z = 3.0$ m the propagation would be approximately linear. After 3.0 m the nonlinearity would become significant and the hot spots would begin to self-focus.

Applying the same argumentation for an input beam power of 25 GW beam leads to the conclusion that local collapse will initiate for a distance $z \geq 2$ m with a spatial pattern as in Fig. 1d. In this case we would expect that eight supercritical hot spots would likely be observed, namely, the four corner spots at 12% (3.0 GW) of the total beam power and the four centered side spots at 9% (2.3 GW). The central spot was right on the borderline at 7% (1.8 GW).

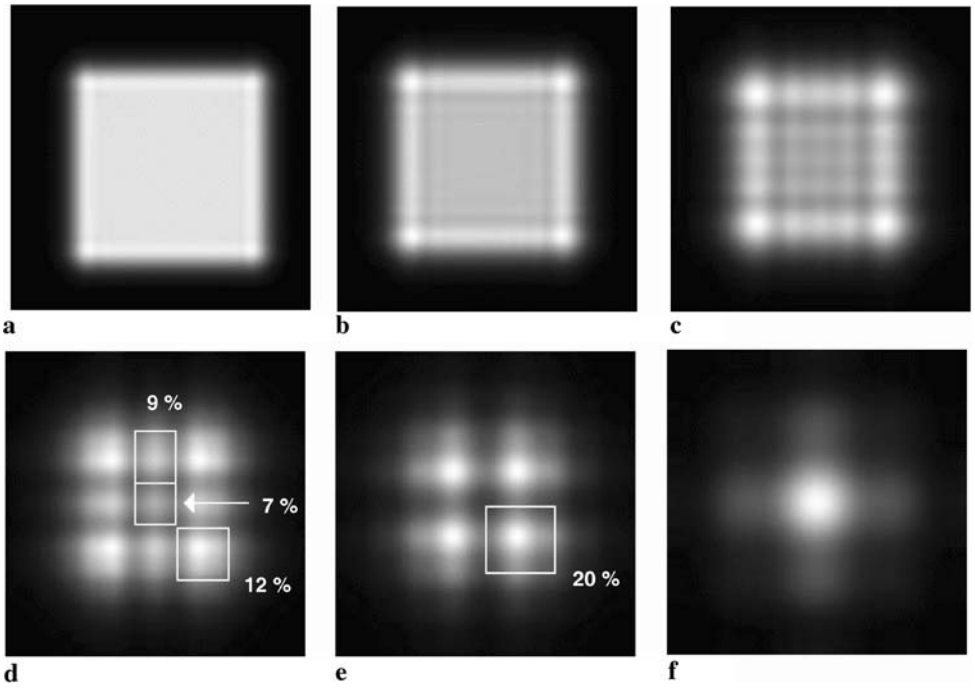


**FIGURE 1** Linear diffraction pattern for square aperture at (**a**) $z = 0.3$ m, (**b**) 0.5 m, (**c**) 1.0 m, (**d**) 2.0 m, (**e**) 3.0 m, and (**f**) 6.0 m. The aperture is $4 \times 4\,\text{mm}^2$ and the entire computational domain (not shown) is $20 \times 20\,\text{mm}^2$. In (**d**) roughly 12% of the beam power is contained in each corner lobe, 9% is contained in each centered side lobe and 7% is contained in the central region. In (**e**) about 20% of the beam power is concentrated in each lobe

Also, it was possible to determine the order in which the spots would increase in intensity. For the 9.2 GW beam, we expected all four spots to increase in intensity at the same rate. However, for the 25 GW beam, we expected the corner spots to self-focus most quickly, followed by the center side spots. If there was sufficient power in the central spot to cause it to self-focus, we expected to see it focus last.

Figures 2 and 3 show the results of simulating a $4 \times 4\,\text{mm}^2$ nonlinear beam at 9.2 GW and 25 GW, respectively. These powers correspond to peak intensities of $6.7 \times 10^{14}\,\text{Wm}^{-2}$ and $1.8 \times 10^{15}\,\text{Wm}^{-2}$, respectively. The figures show that, indeed, the power was partitioned in the beams in a way that suggested that each of the beams underwent quasi-linear diffractive propagation in the early stages of the simulation. As expected in Figs. 2b and 3c the corner hot spots contain

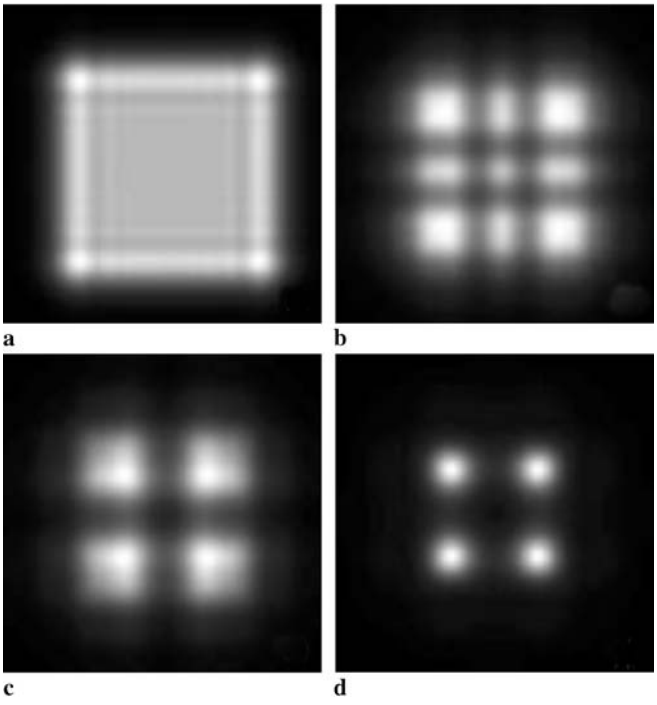


**FIGURE 2** Intensity profiles of 9.2 GW square beam at (**a**) $z = 0.5$ m, (**b**) 2.0 m, (**c**) 3.0 m, and (**d**) 4.0 m. The aperture is $2 \times 2\,\text{mm}^2$, and the entire computational domain (not shown) is $20 \times 20\,\text{mm}^2$

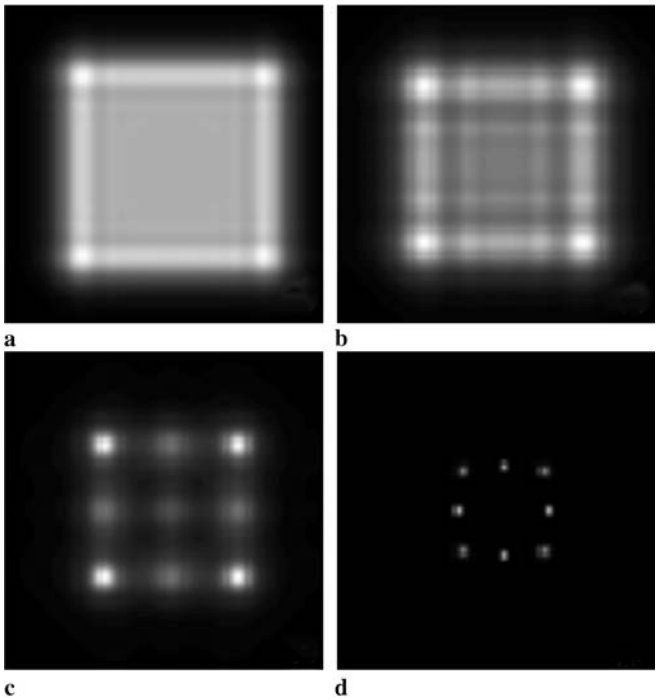


**FIGURE 3** Intensity profiles for the nonlinear propagation of an input square beam of 25 GW beam at (**a**) $z = 0.5$ m, (**b**) 1.0 m, (**c**) 2.0 m, and (**d**) 6.0 m. The aperture is $2 \times 2\,\text{mm}^2$, and the entire computational domain (not shown) is $20 \times 20\,\text{mm}^2$. The corner filaments collapsed first. Kerr saturation was used after frame (**c**) to propagate past the collapse distances of the corner filaments to allow the side filaments to self-focus

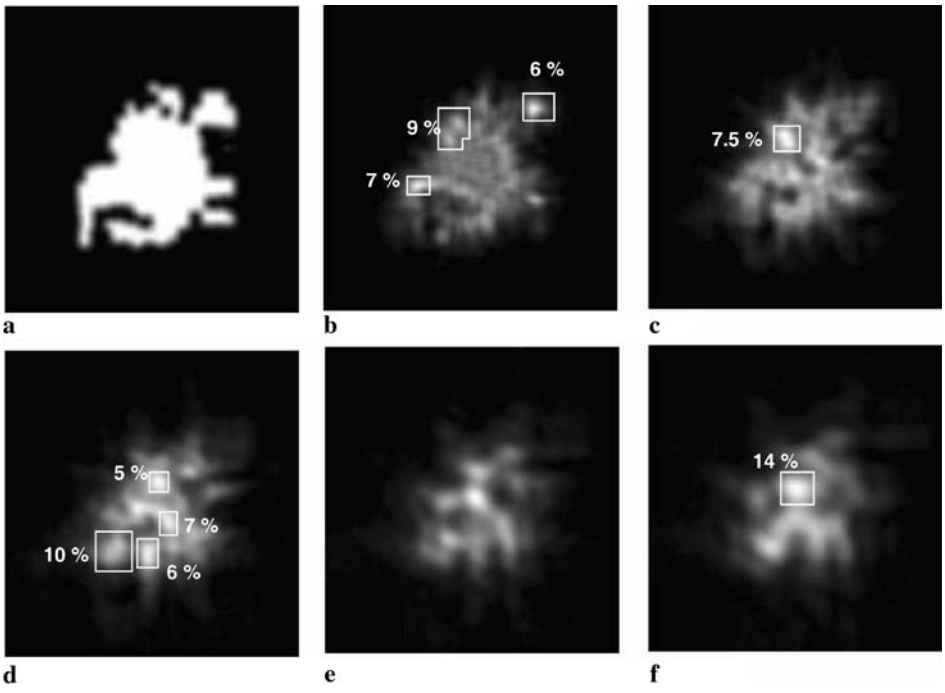


**FIGURE 4** Linear diffraction pattern from an irregular aperture. (**a**) Input at $z = 0$ m, (**b**) 0.5 m, (**c**) 1.0 m, (**d**) 1.6 m, (**e**) 2.1 m, and (**f**) 2.7 m

14% of the total power, the center-side spots contain 8% of the total power and the center spot contains 5% of the total power. Also, the spots in Fig. 3d collapsed in the order predicted by quasi-linear analysis. It should be noted that the Kerr saturation model was employed for the 25 GW beam in order to allow the center side spots to collapse. There was no evidence of the central spot surviving past $z = 6.0$ m.

### 3.2 *Irregular aperture*

In order to more generally demonstrate the utility of linear partitioning of the power for supercritical beams, cw simulations were performed with an irregular aperture. The shape of the irregular aperture is shown in Fig. 4a, the intensity being constant in the white area and zero outside. The remaining plots b–f show the linear diffraction patterns for the irregular aperture at propagation distances between 0–2.7 m. The computation domain was $20 \times 20\,\text{mm}^2$ on a numerical grid of $512 \times 512$ points. The boxes in b, c and d show the locations of and the fraction of the total beam power contained in several potential hot spots.

First, the nonlinear intensity was selected so that the critical power would occur at about 6% of the total beam power. In the case of the aperture shown in Fig. 4a this occurred at an intensity of $3.3 \times 10^{15}\ \text{Wm}^{-2}$ (30 GW). Linear power partitioning then predicts that the three hot spots indicated in Fig. 4b for $z \geq 0.5$ m should form self-focusing hot spots. The results of propagating the nonlinear beam are shown in Fig. 5 and verify that the linear partitioning approach predicts the locations of the hot spots. The first spot to begin self-focusing was the 6% spot. This spot was nearly bell-shaped initially, which led to early self-similar collapse. The 7% spot started out somewhat elongated. Therefore, it underwent diffraction before becoming bell-shaped and succumbing to self-collapse later in the simulation. The 9% spot was initially two spots that had to merge before the self-focusing would dominate.

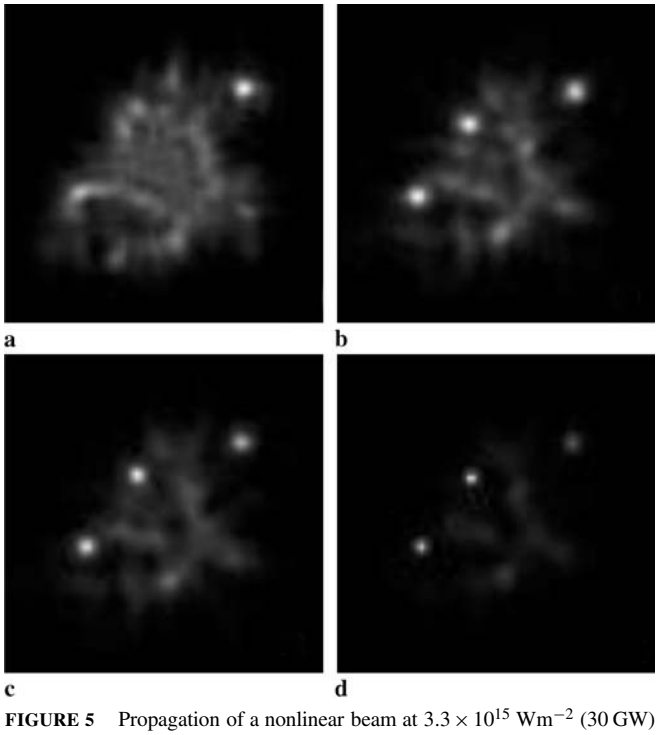


**FIGURE 5** Propagation of a nonlinear beam at $3.3 \times 10^{15}\ \text{Wm}^{-2}$ (30 GW) through an irregular aperture. (**a**) $z = 0.5$ m, (**b**) 1.0 m, (**c**) 1.1 m, and (**d**) 1.3 m. Compare to Fig. 4b

As a further test we considered a 13 GW input beam, for which a hot spot would have to contain about 14% of the total power to be critical. According to linear analysis this occurs at about $z = 2.7$ m (Fig. 4f). Figure 6 shows the intensity profiles of the lower powered beam through the same irregular aperture, and again the results of the nonlinear simulation were consistent with the initial stages of the beam propagation being dominated by linear diffraction.

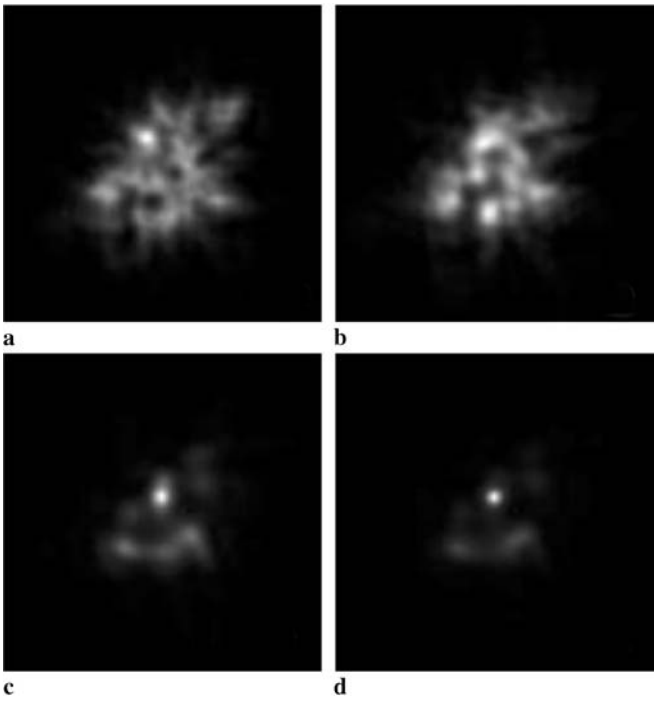


**FIGURE 6** Propagation of a nonlinear beam at $1.4 \times 10^{15}$ Wm$^{-2}$ (13 GW) through an irregular aperture. (**a**) $z = 1.0$ m, (**b**) 1.7 m, (**c**) 2.7 m, and (**d**) 2.9 m. Compare to Fig. 4f

### 3.3 *Hamiltonian analysis of continuous wave simulations*

It is instructive to compare the quasi-linear cw results with the predictions of Hamiltonian analysis. The Hamiltonian for the square beam in air was derived by inserting (10) into (2) with the result

$$H^{\mathrm{SG}} = \frac{|E_0|^2}{8\,k^2}\left\{2\,\Gamma\left(\frac{4m-1}{2m}\right)\Gamma\left(\frac{1}{2m}\right) - \pi\frac{P^{\mathrm{SG}}}{P_{\mathrm{cr}}}\right\}, \qquad (11)$$

where $P^{\mathrm{SG}}$ is the total beam power, $P_{\mathrm{cr}}$ is the critical power of a Gaussian beam, and $\Gamma(\xi)$ is the standard gamma function. For super-Gaussian orders $m > 5$ we may reasonably approximate the beam Hamiltonian and power as

$$H^{\mathrm{SG}} = \frac{m|E_0|^2}{2\,k^2}\left\{1 - \frac{P^{\mathrm{SG}}}{P_{\mathrm{cr}}^{\mathrm{SG}}}\right\}, \qquad (12)$$

$$P^{\mathrm{SG}} = \frac{|E_0|^2 d^2\,\Gamma^2(1/2m)}{m^2 2^{1/m}}, \qquad (13)$$

where we have introduced the critical power $P_{\mathrm{cr}}^{\mathrm{SG}}$ for global collapse of the super-Gaussian field as

$$P_{\mathrm{cr}}^{\mathrm{SG}} = \frac{2m}{\pi}P_{\mathrm{cr}}\,. \qquad (14)$$

Using (14) we find that $P_{\mathrm{cr}}^{\mathrm{SG}} = 9.2$ GW, meaning that the simulation for an input beam power of 25 GW beam was globally supercritical. This becomes clear upon examination of Fig. 3 which shows that the square pattern of hot spots contracts as the beam propagates, thus displaying global collapse. Furthermore, in Fig. 7a, which shows the RMS radius of the power distribution for three square beams of different powers (25 GW, 9.2 GW, and 8.8 GW), the RMS radius of the 25 GW beam is seen to reduce, indicating global collapse. The critical and subcritical beams (9.2 GW and 8.8 GW) did not undergo critical collapse in the global sense in that their RMS radii remained relatively constant or increased with propagation distance as shown in Fig. 7a. However, both still contained hot spots that experienced local collapse as predicted by linear analysis.

Figure 7b shows the RMS radius versus propagation distance for the irregular aperture for the input powers of 13 GW and 30 GW previously discussed, and a higher power case (75 GW) that was performed as a comparison. The Hamiltonian was calculated numerically for the irregular aperture and the critical power for global collapse was determined to be 30 GW, so the 13 GW was globally subcritical. The 30 GW beam was very close to critical so it could globally collapse or globally spread. This was consistent with the behavior of the RMS radii for these beams shown in Fig. 7b, where the RMS radii are seen to increase in both cases. In contrast, the 75 GW beam was globally supercritical and its RMS radius decreases as a function of propagation distance.

## 4 Pulse simulations

So far the linear power partitioning approach has yielded good results for high power apertured cw beams. However, whether it will be a useful technique for understanding real filamentation phenomena in nonlinear pulses has yet to be established. To explore this, space-time simulations in $(3+1)$ dimensions were performed for the two apertures of the previous sections. For these simulations the extended NLS for the electric field envelope $E(\boldsymbol{r}, z, t)$ in a reference frame moving at the group velocity is written as [10]

$$\frac{\partial E}{\partial z} = \frac{\mathrm{i}}{2k}\nabla_t^2 E - \mathrm{i}\frac{\beta_2}{2}\frac{\partial^2 E}{\partial t^2} - \mathrm{i}\frac{\sigma}{2}\omega\tau\varrho E + \mathrm{i}k_0 n_2|E|^2 E - \frac{1}{2}\kappa\hbar\omega B^{(\kappa)}|E|^{2\kappa-2}E\,, \qquad (15)$$

where $t$ refers to the local time within the pulse, the first term on the right-hand side describes beam diffraction as before, the second term describes GVD, the third term accounts for plasma induced defocusing, the fourth is the nonlinear Kerr effect as before, and the fifth term describes nonlinear absorption due to multi-photon ionization (MPI). For all of the pulse simulations the definitions and values of the parameters were as follows

- $k$ (wavenumber, $n_{\mathrm{b}}\omega/c$): $7.96 \times 10^6$ m$^{-1}$
- $\omega$ (angular frequency of light)
- $\beta_2$ (coefficient of GVD): 0.3 fs$^2$cm$^{-1}$
- $\sigma$ (coefficient of inverse bremsstrahlung): $5.32 \times 10^{-24}$ m$^2$
- $\tau$ (mean time between electron-neutral collisions): $3.5 \times 10^{-13}$ s
- $\varrho$ (plasma density)
- $n_2$ (nonlinear index of refraction): $5.57 \times 10^{-23}$ m$^2$W$^{-1}$

The associated equation for the plasma density is [10]

$$\frac{\partial \varrho}{\partial t} = B^{(\kappa)}|E|^{2\kappa} - \alpha\varrho^2\,, \qquad (16)$$

where the first term on the right hand side describes the generation of electrons due to MPI of order $\kappa$, and the second

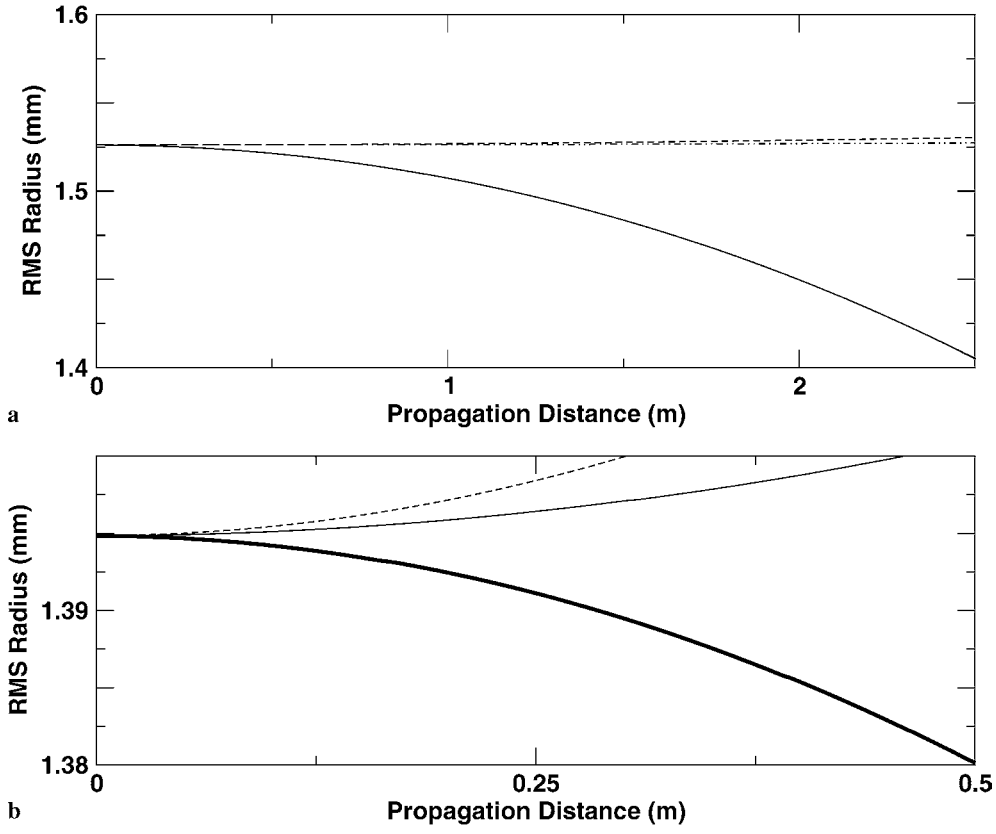


**FIGURE 7** Overall RMS spot radius as a function of propagation distance for (**a**) the square aperture and (**b**) the irregular aperture. In (**a**) a 24.5 GW beam (solid line), a 9.2 GW beam (*dotted-dashed line*) and a 8.8 GW beam (*dashed line*) are shown. In (**b**) a 13 GW beam (*dashed line*), a 30 GW beam (*solid line*) and a 75 GW beam (*bold line*) are shown

term describes non-radiative recombination. The parameters employed in the simulations were

- $\kappa$ (MP order): 8
- $B^{(\kappa)}$ (MPI coefficient): $1.3 \times 10^{-106}\ \mathrm{s^{-1}m^{16}W^{-8}}$
- $\alpha$ (recombination coefficient): $5.0 \times 10^{-13}\ \mathrm{m^3 s^{-1}}$

### 4.1 *Pulses through a square aperture*

Due to numerical constraints for the pulse simulations the aperture and numerical grids needed to be shrunk in size. Again, the super-Gaussian model was used for the aperture, as in the cw simulations, and a Gaussian pulse profile was added. The aperture dimensions were reduced to $0.5 \times 0.5\ \mathrm{mm^2}$, and the duration of the pulse was chosen as $t_\mathrm{p} = 120$ fs. The total computational domain (not shown) was $(5 \times 5\ \mathrm{mm^2}) \times 650$ fs on a $(256 \times 256) \times 512$ computational grid.

Figure 8 shows the fluence profiles for a low power pulse propagating through the square aperture. Notice that Fig. 8b–d correspond with Fig. 1d–f, respectively. Since the aperture dimensions were scaled by a factor of 1/8 in comparison to those in Fig. 1, the propagation distances were scaled by 1/64 so that the simulations corresponded to the same effective Fresnel number. To allow comparison between the cw and pulse simulations, we calculated the spatial profile of the fluence $F(x, y, z)$ as the time integrated intensity at the selected plane $z$. Taking into account the scale factor in the spatial dimensions, we found the fluence profiles in Fig. 8 to have their average power partitioned in much the same way as the power was in the linear cw case. That is, in Fig. 8b about 20% of the fluence was contained in each of the four lobes of the cross section. In Fig. 8c about 11% was contained in the corner spots, 10% was contained in the center side spots, and 8% was contained in the central region.

Two high power pulses (1.7 mJ and 3.5 mJ) were propagated through the square aperture. These corresponded to pulses with peak powers of 21 GW and 43 GW, respectively, and average powers of 14 GW and 28 GW, respectively. The average power was calculated by dividing the spatially integrated fluence by $\sqrt{\frac{\pi}{2}}t_\mathrm{p}$ which is the equivalent integrated width of a Gaussian temporal pulse with 1/e width of $t_\mathrm{p}$. The resolution was different from that of the linear case. The aperture was still $0.5 \times 0.5\ \mathrm{mm^2}$. However, the temporal duration of the pulse was decreased to $t_\mathrm{p} = 65$ fs. Also, the computational domain was decreased to $(2.5 \times 2.5\ \mathrm{mm^2}) \times 650$ fs on a $(256 \times 256) \times 512$ computational grid.

We would expect the behavior of the filaments to be dominated by the average power in each filament rather than the peak power. If this is the case, then the 1.7 mJ pulse should evolve similarly to the 9.2 GW cw square beam case and the 3.5 mJ pulse is similar to the 28.9 GW cw square beam case. Therefore we expect to see fluence patterns develop that are similar to the intensity profiles shown in Figs. 2 and 3. We see in Figs. 9 and 10 that this is indeed the case.

In Figs. 9b and 10b, the fraction of the average beam power was distributed the same way. About 14% was contained in each corner lobe, 8% was contained in each center side lobe and 5% was contained in the central region. This distribution would make the 3.5 mJ pulse supercritical in each of the outside filaments and the 1.7 mJ pulse would be supercritical only in the corner filaments. These results are in good agreement with the linear pulsed and cw cases.

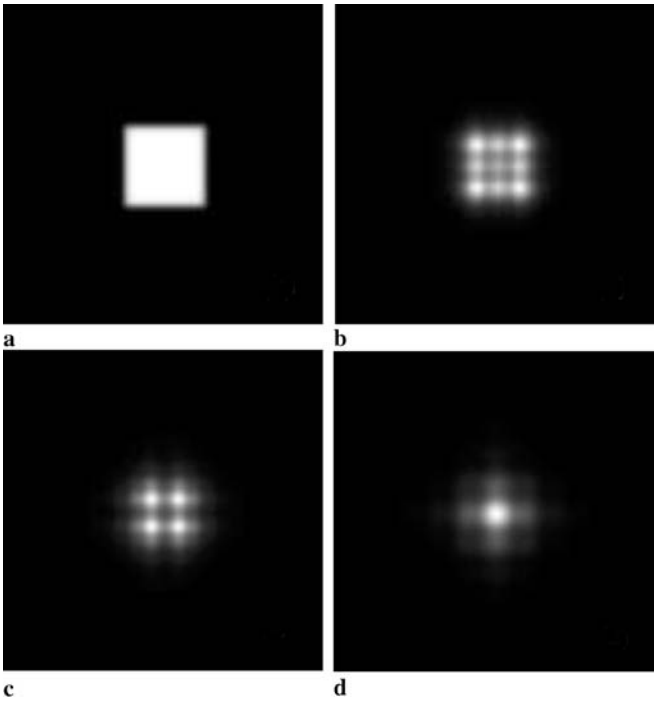


**FIGURE 8** Fluence profiles of linear pulse through a square aperture. The aperture is $0.5 \times 0.5$ mm$^2$ and the pulse has a duration of 120 fs. Only the central region of the computational domain is shown. (**a**) $z = 0.0$ cm, (**b**) 2.5 cm, (**c**) 5.0 cm, (**d**) 9.2 cm

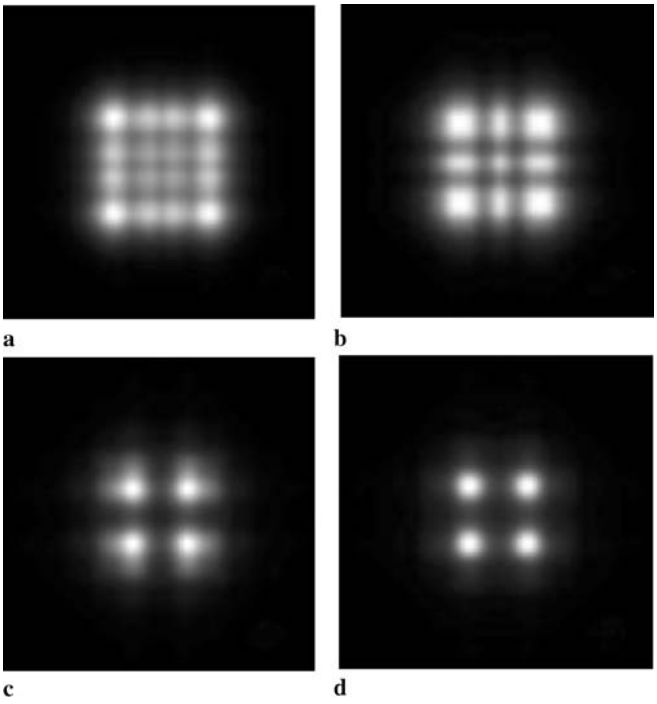


**FIGURE 9** Fluence profiles for 1.7 mJ pulse at (**a**) $z = 2.0$ cm, (**b**) 3.0 cm, (**c**) 5.1 cm, and (**d**) 6.1 cm. Compare to Fig. 8c. Only the region of the computational domain immediately surrounding the beam is shown. The region shown is approximately $1 \times 1$ mm$^2$

Comparing Figs. 9b and 10b, self focusing was apparent at this stage in the 3.5 mJ pulse. This is seen as a slightly more defined fluence pattern in the 3.5 mJ case. Going on to Figs. 9c and 10c, the 1.7 mJ pulse underwent an additional amount of linear diffraction, forming four lobes each containing about 22% of the average pulse power. At this stage, each of the four lobes was supercritical and self-focusing became evident in 9d. By Fig. 10c, the 3.5 mJ pulse was clearly out of the quasi-linear propagation regime. The complex patterns displayed in Fig. 10c and d resulted as the closely spaced filaments began to interact and merge.

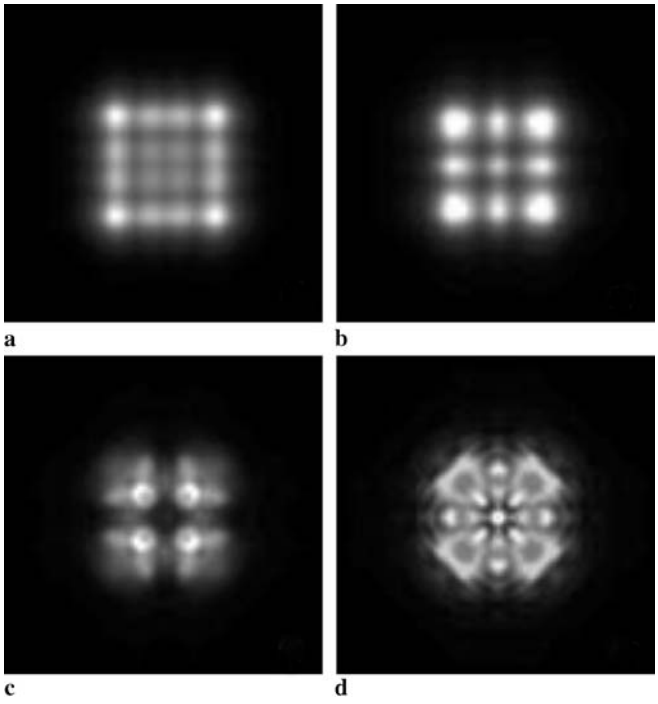


**FIGURE 10** Fluence profiles for 3.5 mJ pulse at (**a**) $z = 2.0$ cm, (**b**) 3.1 cm, (**c**) 5.1 cm, and (**d**) 6.1 cm. Only the region of the computational domain immediately surrounding the beam is shown. The region shown is approximately $1 \times 1$ mm$^2$

### 4.2 *Pulses through an irregular aperture*

Figures 11 and 12 show the fluence profiles for two different pulse energies (1.1 mJ and 2.5 mJ, respectively) after propagating through the irregular aperture. These energies corresponded to an average power of 13 GW and 28 GW, respectively. Again the computational domain was scaled down by a a factor of $1/2$ compared to the cw simulation. Therefore, in order to compare with the cw simulations, the distances over which the pulses were simulated were scaled by a factor of $1/4$ so that all simulations had approximately the same Fresnel number. The domain measured $(10 \times 10\,\text{mm}^2) \times 650$ fs on a $(256 \times 256) \times 512$ numerical grid.

In both cases, the behavior is similar to that seen for the cw cases shown in Figs. 5 and 6. In the case of the 1.1 mJ pulse, a single supercritical filament forms at the position predicted by linear analysis (Fig. 11d). The 2.5 mJ pulse forms at least three supercritical filaments (Fig. 12d) all at positions consistent with those predicted by linear analysis.

## 5 Conclusion

We have demonstrated through numerical simulation that linear diffraction plays an important role in partitioning the power in apertured beams. Our results show that for high power apertured beams, linear analysis can be used

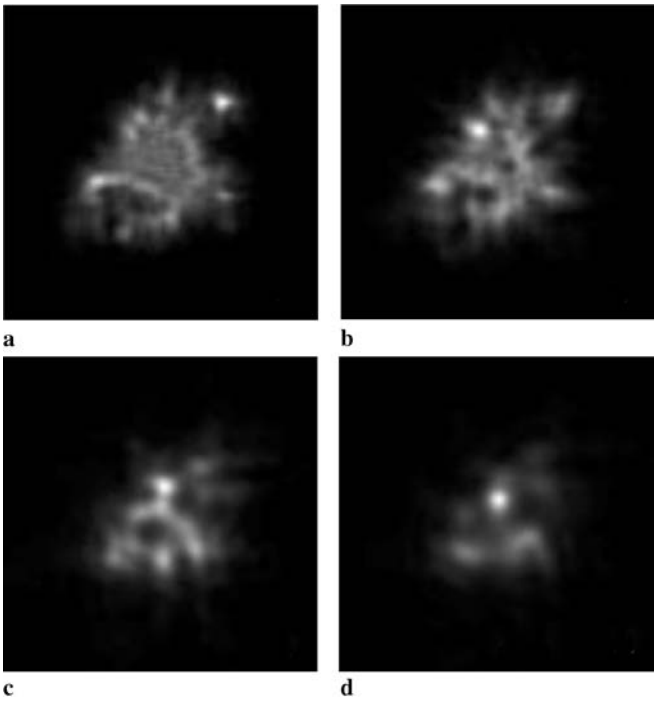


**FIGURE 11** Fluence patterns for 1.1 mJ (13 GW) pulse at (**a**) 12.6 cm, (**b**) 25.2 cm, (**c**) 53.1 cm, and (**d**) 68.2 cm. Only the region of the computational domain immediately surrounding the beam is shown. The region shown is approximately $3 \times 3\ \mathrm{mm}^2$

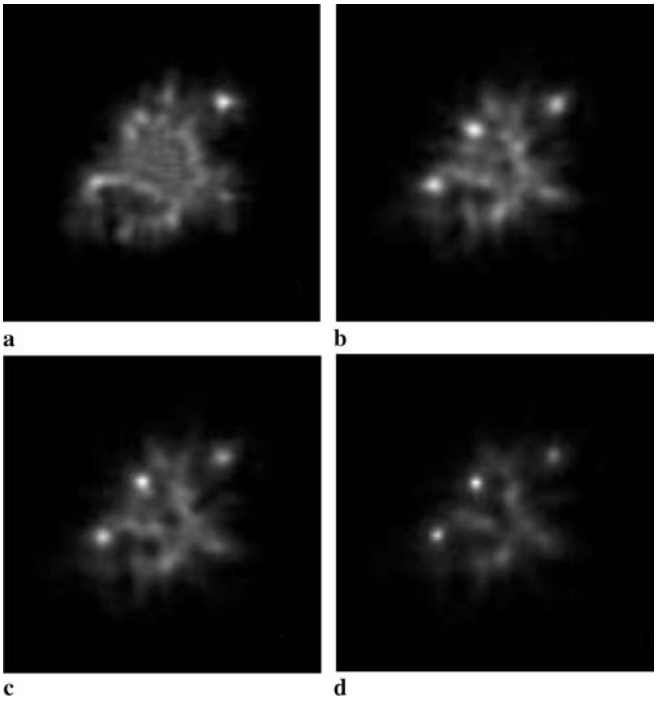


**FIGURE 12** Fluence patterns for 2.5 mJ (28 GW) pulse at (**a**) $z = 12.6$ cm, (**b**) 25.1 cm, (**c**) 27.6 cm, and (**d**) 32.6 cm. Only the region of the computational domain immediately surrounding the beam is shown. The region shown is approximately $3 \times 3\ \mathrm{mm}^2$

to accurately predict the location and relative intensities of multiple hot spots. The beam power is partitioned by linear diffraction into what will later become self-guiding hot spots. Once a hot spot contains a critical power or more, it begins to exhibit strong nonlinear phenomena, marking the end of quasi-linear propagation. Given a large enough beam, these hot spots can propagate in a relatively independent fashion over an extended distance. In fact, linear propagation can continue in locally subcritical portions of a wide beam even while critical collapse is occurring in another region. Linear analysis enabled us to explore, in more detail than afforded by Hamiltonian and MI analyses, how a nonlinear beam was likely to break up into multiple hot spots and how the total beam power would be distributed over those spots.

We have also demonstrated that linear power partitioning occurs in short pulses. Simulations were performed that showed short, high power pulses undergoing quasi-linear propagation before exhibiting distinctly nonlinear behavior. In fact, the qualitative behavior and, to a good approximation, the quantitative behavior of the nonlinear pulses during the initial quasi-linear regime did not deviate much from the behavior of linear cw beams. This is a very useful observation for diagnosing filamentation patterns in real nonlinear systems.

The simulations described in this paper involved apertures with relatively hard edges. However, we contend that linear effects initially dominate in a broad range of high power systems. For instance, aberrations might linearly partition power into multiple filaments in complex femtosecond laser systems. Furthermore, quasi-linear analysis might be useful in describing the behavior of nonlinear Bessel–Gauss beams and subcritical circularly apertured beams which exhibit anomalous self-guiding behavior [33]. Also, linear power partitioning would be a dominant effect in high power beams with strong phase aberrations such as those that can be created by computer generated holograms, diffractive optical elements, phase plates or exotic lens-like optics such as axicons.

Finally, we remark that since single light filaments can only carry limited energy; it is, therefore, important to understand how organized arrays of filaments can be formed to boost energy transport in ultrashort pulses and long distance propagation. Analysis based on linear power partitioning may provide a means to realize this goal.

**ACKNOWLEDGEMENTS** D.E. Roskey would like to thank the Directed Energy Professional Society for a graduate scholarship that supported his work over the past three years.

This work was also supported by the Air Force Office for Scientific Research under grants F49620-03-1-0194, FA9550-04-1-0213, FA9550-04-1-0355, and by the NLWD under grant M67854-06-1-5005.

## REFERENCES

1 J.H. Marburger, Prog. Quantum Electron. **4**, 35 (1975)
2 P. Monot, T. Auguste, L.A. Lompré, G. Mainfray, C. Manus, J. Opt. Soc. Am. B **9**, 1579 (1992)
3 P. Chernev, V. Petrov, Opt. Lett. **17**, 172 (1992)
4 J.K. Ranka, R.W. Schirmer, A.L. Gaeta, Phys. Rev. Lett. **77**, 3783 (1996)
5 J.J. Rasmussen, K. Rypdal, Phys. Scripta **33**, 481 (1986)
6 L. Bergé, J.J. Rasmussen, E.A. Kuznetsov, E.G. Shapiro, S.K. Turitsyn, J. Opt. Soc. Am. B **13**, 1879 (1996)
7 A. Braun, G. Korn, X. Liu, D. Du, J. Squier, G. Mourou, Opt. Lett. **20**, 73 (1995)
8 A. Brodeur, C.Y. Chien, F.A. Ilkov, S.L. Chin, O.G. Kosareva, V.P. Kandidov, Opt. Lett. **22**, 304 (1997)
9 H.R. Lange, G. Grillon, J.-F. Ripoche, M.A. Franco, B. Lamouroux, B.S. Prade, A. Mysyrowicz, E.T.J. Nibbering, A. Chiron, Opt. Lett. **23**, 120 (1998)

10 M. Mlejnek, E.M. Wright, J.V. Moloney, Opt. Lett. **23**, 382 (1998)
11 M. Mlejnek, E.M. Wright, J.V. Moloney, IEEE J. Quantum Electron. **QE-35**, 1771 (1999)
12 S. Tzortzakis, L. Bergé, A. Couairon, M. Franco, B. Prade, A. Mysyrowicz, Phys. Rev. Lett. **86**, 5470 (2001)
13 A.J. Campillo, S.L. Shapiro, B.R. Suydam, Appl. Phys. Lett **24**, 178 (1974).
14 L. Bergé, C. Gouédard, J Schjødt-Eriksen, H. Ward, Physica D **176**, 181 (2003)
15 L. Bergé, S. Skupin, F. Lederer, G. Méjean, J. Yu, J. Kasparian, E. Salmon, J.P. Wolf, M. Rodriquez, L. Wöste, R. Bourayou, R. Sauerbrey, Phys. Rev. Lett. **92**, 225 002 (2004)
16 G. Fibich, S. Eisenmann, B. Ilan, Y. Erlich, M. Fraenkel, Z. Henis, A.L. Gaeta, A. Zigler, Opt. Express **13**, 5897 (2005)
17 K.D. Moll, A.L. Gaeta, G. Fibich, Phys. Rev. Lett. **90**, 203 902 (2003)
18 G. Méchain, A. Couairon, M. Franco, B. Prade, A. Mysyrowicz, Phys. Rev. Lett. **93**, 035 003 (2004)
19 V.P. Kandidov, N. Akozbek, M. Scalora, O.G. Kosareva, A.V. Nyakk, Q. Luo, S.A. Hosseini, S.L. Chin, Appl. Phys. B **80**, 267 (2004)
20 K. Cook, A.K. Kar, R.A. Lamb, Opt. Express **13**, 2025 (2005)
21 G. Fibich, S. Eisenmann, B. Ilan, A. Zigler, Opt. Lett. **29**, 1772 (2004)
22 O.G. Kosareva, N.A. Panov, N. Akozbek, V.P. Kandidov, Q. Luo, S.A. Hossenini, W. Liu, J.-F. Gravel, G. Roy, S.L. Chin, Appl. Phys. B **82**, 111 (2005)
23 A.J. Campillo, J.E. Pearson, S.L. Shapiro, N.J. Terrell Jr., Appl. Phys. Lett. **23**, 85 (1973)
24 P. Johannisson, D. Anderson, M. Lisak, M. Marklund, Opt. Commun. **222**, 107 (2003)
25 S.L. Chin, A. Talebpour, J. Yang, S. Petit, V.P. Kandidov, O.G. Kosareva, M.P. Tamarov, Appl. Phys. B **74**, 67 (2002)
26 D.L. Fried, J. Opt. Soc. Am. **55**, 1427 (1965)
27 D.L. Fried, J. Opt. Soc. Am. **56**, 1372 (1966)
28 L.C. Andrews, R.L. PHillips, *Laser Beam Propagation through Random Media* (SPIE Press, USA, 1998)
29 S.L. Chin, A. Talebpour, J. Yang, S. Petit, V.P. Kandidov, O.G. Kosareva, M.P. Tamarov, Appl. Phys. B **74**, 67 (2001)
30 V.P. Kandidov, V.O. Militsin, Appl. Phys. B **83**, 171 (2006)
31 P.L. DeVries, *A First Course in Computational Physics* (Wiley, USA, 1994)
32 R.W. Boyd, *Nonlinear Optics* (Academic Press, 1992)
33 C. Ruiz, J. San Román, C. Méndez, V. Díaz, L. Plaja, I. Arias, L. Roso, Phys. Rev. Lett. **95**, 053 905 (2005)